Near-Infrared Activated Liposomes for Neuroprotection in Glaucoma

Dorcas Matuwana¹, Eunji Hong¹, Sizhe Huang¹, Xinxin Xu¹, Geunho Jang¹, Ruobai Xiao¹, Siyuan Rao^{1,2*}, Qianbin Wang^{1*}

- 1. Department of Biomedical Engineering, Binghamton University, Binghamton, NY 13902, USA
- 2. Integrative Neuroscience Program, Binghamton University, Binghamton, NY 13902, USA

Corresponding authors: Siyuan Rao (syrao@binghamton.edu), Qianbin Wang (qbwang@binghamton.edu),

Abstract:

Neurodegenerative diseases have a profound impact on vision, leading to conditions such as glaucoma, optic neuropathy, and diabetic retinopathy, affecting millions worldwide. These diseases are characterized by the degeneration of retinal ganglion cells (RGCs), resulting in a progressive loss of visual acuity and field, with the threat of irreversible blindness. However, existing treatments, such as eye drops, direct injections, and laser surgeries face significant challenges due to limited efficacy and potential infection. The inefficiency of traditional corneal drug delivery methods is a major obstacle in treating vision neurodegenerative diseases. To address these challenges, we developed a remotely triggered on-demand liposomal delivery system to treat glaucomatous neurodegeneration in mice. We utilized the localized surface plasmon resonance (LSPR) effect of gold nanorods (AuNRs) under near-infrared (NIR) light (808nm) to control the release of cyclodextrin-encapsulated melatonin from thermally responsive liposomal nanocarriers in the vitreous humor. Due to the transparency of eye corneal, NIR light can penetrate deep tissues, enabling on-demand drug delivery to the retina. By enhancing the drug's solubility and stability through cyclodextrin encapsulation, this remotely activated melatonin/HPBCD AuNRs liposomes delivery system can decrease intraocular pressure (IOP) elevation by (24 ± 7) %, enhance the survival rate of RGCs by (77±6) %, and decrease glial fibrillary acidic protein (GFAP) activation by (75±6) % at depth in an acute experimental glaucoma model. This NIR-triggered drug delivery system presents the potential of a promising minimally photo-triggered therapeutic option for glaucoma treatment.

Introduction

Glaucoma is a critical group of eye conditions characterized by the degeneration of the optic nerve, which is essential in transmitting visual information from the eye to the brain.¹ Often associated with elevated intraocular pressure (IOP), this condition poses a significant risk of irreversible blindness if left untreated. Elevated IOP impairs the drainage of ocular fluid, leading to retinal degeneration and optic neuropathy.² Over time, this pressure damages retinal ganglion cells (RGCs) and the optic nerve, disrupting the communication between the eye and brain, and causing progressive vision loss.³ Contemporary therapeutic strategies aim to mitigate the progression of glaucoma by concentrating on the primary modifiable risk factor: the reduction of IOP.⁴ While these conventional treatments, such as eyedrops⁵, laser therapy⁶ and surgical procedures⁷, can preserve visual function by halting the neurodegenerative process, their application presents significant limitations.

Conventional glaucoma treatments, whether non-invasive or surgical, face significant limitations and risks. Eyedrops, such as GSH-functionalized hydrogels⁸, hollow mesoporous ceria nanoparticles (HMCNs)⁹, and bioadhesive polymer-based timolol¹⁰, offer sustained drug release to ocular tissue but still struggle with limited drug absorption due to corneal and conjunctival barriers. On the other hand, traditional methods of direct injection, such as the administration of anti-vascular endothelial growth factor (anti-VEGF) injections, while effective, are invasive, require frequent administration, and pose risks of infection and retinal detachment.⁴ Similarly, although laser surgeries are useful in reducing IOP, these can result to side effects such as the loss of peripheral or night vision. Additionally, surgical options like trabeculectomy come with complications such as scarring, infection, and the need for repeat surgeries.⁴ In light of these limitations, recent advances in pharmacological treatments have focused on developing more efficient drug delivery systems that maintain therapeutic levels over time while minimizing side effects.

Effective pharmacological delivery methods aim to maintain consistent therapeutic levels over time while minimizing the frequency of dosing¹¹. Based on the release dynamics, sustained drug delivery systems offer a continuous payload release¹¹, which is enabled by surface modification and structural design of nanomaterials, such as aminated-chitosan-coated ceria nanocapsules², gelatin-functionalized mesoporous silica nanoparticles¹², and poly(ε-caprolactone) nanocapsules¹³; these systems often lack precise control over timing and dosage. Controllable delivery systems, on the other hand, offer more refined regulation of drug release dynamics. Certain physiological parameters, such as temperature, pH and enzyme activity, offer natural stimuli for controllable release¹⁴. As temperature-responsive carriers, hydrogel substrates made from poly(N-isopropyl acrylamide) or its grafted derivatives have the advantage of volumetric change from room temperature to physiological temperatures to enable drug release¹⁵⁻¹⁷. When local

physiological pH changes, designed carriers with chitosan or polyacrylic acid (PAA) exhibited polymer chain conformation changes through protonation and release payload¹⁸; with enzyme activation, certain ester or amide bonds are cleaved and consequently breakdown of the polymeric matrix and release embedded drug sustainably¹⁹. Integrating these mechanisms with external, non-invasive stimuli such as light²⁰, magnetic fields²¹, and ultrasound²² adds additional convenience of programmable release control. These combinations allow for enhanced temporal precision in drug delivery, making these advanced systems highly effective for targeted therapeutic applications.

In the realm of non-invasive treatments, light-assisted phototherapy, particularly in the NIR spectrum of 700 to 1,000 nm²³, offers an effective approach for deep tissue treatment²⁴. Utilizing NIR light as a trigger, this method facilitates localized, yet sustained drug delivery directly to the retinal tissues, providing a non-invasive strategy for glaucoma management²⁵. Compared to other remotely controlled drug delivery approaches²⁶, and given the cornea's transparency and the eye's dynamic fluid circulation, NIR optical stimuli present as an ideal choice for their deep tissue penetration, straightforward experimental setup, rapid response time, and compatibility with the eye's natural processes, without compromising the integrity of vision.²⁴

The localized surface plasmon resonance (LSPR) effect on metallic nanoparticles, which generates heat through surface electron oscillations and electron-photon interactions upon light exposure, further enhances this approach.^{27, 28} By applying the thermal effect from nanoparticles' LSPR, particularly within the deep-penetration NIR wavelength range, to thermally responsive liposomal nanocarriers, we design a remotely controlled mechanism for on-demand local drug release. The NIR optical stimulus serves as a switch, enabling targeted and controlled release of the encapsulated pharmacological payload.

Here, we developed a NIR-triggered drug release system by leveraging the NIR's penetrative and photothermal capabilities with gold nanorods (AuNRs), and thermally responsive liposomes. Melatonin, a preventative pharmacological hormone for alleviating glaucomatous RGC degeneration²⁹, was chosen as the target compound. To enhance melatonin's solubility and loading efficiency, we used 2-Hydroxypropyl-β-cyclodextrin (HPβCD) to form a melatonin/HPβCD complex and then loaded them within liposomal carriers. With a single injection and subsequent NIR illumination to initiate drug release in mouse models, we assessed the RGC loss and astrocyte activation through the immunohistological examination of mouse retinal tissues. To validate the efficacy, we monitored IOP over time post-injection, as well as the survival rate of RGCs and glial fibrillary acidic protein (GFAP) activation post-injection, serving as a systemic functional outcome. When deploying this method within an acute glaucoma model, we have observed notable reductions (24±7) % in IOP levels, alongside improvements (77±6) % in RGC

preservation, and a reduction (75±6) % in glial activation. This NIR-triggered drug delivery system presents the potential of a promising minimally photo-triggered therapeutic option for glaucoma treatment.

Results and Discussion

Near-Infrared Activated Thermal Response

Inspired by the transparent nature of corneal tissues and LSPR-enabled photothermal effect, we designed a NIR-triggered nanoliposome carrier system for precise intravitreal drug delivery (Fig. 1A). AuNRs were encapsulated into nanoscale lipid carriers, which are designed to respond to temperature change caused by NIR illumination. Upon a single injection into the vitreous humor, these liposomes—containing a melatonin-cyclodextrin complex—remain stable and inert without NIR illumination. When exposed to NIR light ('Laser ON'), the local temperature increase induced by the LSPR effect from the AuNRs facilitates the diffusion of melatonin from the liposomes into the vitreous cavity.

Rod-shaped gold nanoparticles (Fig.1B) were selected for their superior tunable LSPR properties and efficient heat conversion³⁰. This thermal conversion efficiency is key to rapidly triggering the release of encapsulated melatonin with short NIR exposure times. We first measured the absorbance spectrum of AuNRs solutions (Fig. 1C), which showed a peak in the NIR range, aligning with the desired NIR-enabled photothermal therapy application. We then monitored the thermal response of AuNRs solutions to NIR light (808 nm) for 100 seconds, with water as a control (Fig. 1D). The AuNRs solutions (50 μ L) displayed a rapid temperature rise, peaking at approximately a 4 °C change over 100 seconds, while the water sample (50 μ L) showed minimal temperature changes under the same conditions. The differences in temperature increase upon NIR illumination (11.2 mW for 100 seconds) were also visualized through thermal imaging (Fig. 1E).

We then investigated the photothermal effect's dependency on the concentration of AuNR solutions (Fig. 1F). We prepared a series of concentrations of AuNRs solutions (0.925 nM as 1X, 2.313 nM as 2.5X, and 4.625 nM as 5X) and applied NIR illumination (11.2 mW for 100 seconds). The temperature generally rose with increasing AuNR concentration but eventually plateaued. A significant temperature rise occurred at the 5X concentration (4.625 nM), achieving the desired temperature change (approximately 4-5°C) suitable for in vivo applications. Therefore, the AuNR solutions with 5x concentration were selected for further experiments. To explore the relationship between NIR power and the resultant temperature change in AuNRs solutions, we subjected the AuNRs solutions to varying NIR illumination intensity from 0.04 mW to 48.4 mW (Fig. 1G). As the NIR laser power increased, the AuNRs solutions exhibited notable temperature increases, with about

a 12°C rise at the highest power (48.4 mW) for 100 seconds. When the intensity is reduced to 30.1 mW, a notable reduction in temperature change is noted, approximately 8 °C, illustrating the sensitivity of the photothermal effect to laser power. Further reduction of the laser intensity to 11.2 mW yielded a more modest temperature change around 4 °C.

Liposomal Nanocarriers Controlled Release

We and others have established double-emulsion methods^{26, 31} to prepare liposome nanocarriers encapsulating water-soluble payloads. AuNRs, with 45 nm length and 10 nm diameter, were encapsulated into nanoscale lipid carriers with predefined lipid ratio composition of dipalmitoyl phosphatidylcholine (DPPC): cholesterol: 1,2-distearoyl-sn-glycero-3-phosphoethanolamine-N-carboxy(polyethylene glycol)-2000 (DSPE-PEG-2000) of 66.5:28.5:5. We characterized the morphology of pure liposomes without AuNRs encapsulation and AuNRs loaded liposomes through TEM imaging (Fig. 1H and I, left). The TEM images exhibited the spherical nature of the liposomes with individual distribution and the successful incorporation of AuNRs. Together with the particle tracking analysis technique, we measured the nanocarriers size distribution and observed a normal distribution of empty liposome sizes with a mean diameter of 121.7 nm while an upshift in the mean diameter to 141.4 nm post-AuNRs encapsulation (Fig. 1H and I, right). This enlargement could be attributed to the internalized AuNRs, which contribute additional volume and mass to the liposomes, consequently shifting the average size upward when compared to empty liposomes.

We then characterized the controlled release functionality of the AuNRs liposomal nanocarriers. We first selected a fluorescent dye, Calcein, as the indicator to quantify the release kinetics from thermosensitive liposomes. Exposing the Calcein-loaded liposomes to a bulk heating bath over 60 minutes, we monitored both the bath temperature and fluorescence (Fig. 1J, excitation wavelength of 490 nm with emission detection at 520 nm). The release profile, represented by the black curve (Fig. 1J), indicated an escalation in fluorescence whereas the temperature, shown by the blue curve (Fig. 1J), rises from 37°C to 42°C. The inflection point in Calcein release aligns with the temperature surpassing 37°C, implying a temperature sensitivity of the liposomal membrane. The direct correlation between the ascending temperature and the fluorescence signal indicates the critical role of elevated temperatures in facilitating the permeability and subsequent release of contents from thermosensitive liposomes.

After confirming the temperature-dependent release from liposomes, we investigated the NIR-triggered release. Shifting from bulking heating (Fig. 1J), we exposed Calcein (Fig. 1K) to NIR illumination with a variety of illumination times, ranging from 100 to 400 seconds. Fluorescence intensity was monitored for

the Calcein-encapsulated liposome solution. The release profile indicated a gradual increase in fluorescence intensity as the exposure time to NIR increased, with the most notable increase observed between 300 to 400 seconds, suggesting a cumulative effect of NIR exposure on the release mechanism. The consistent release profile along with prolonged NIR exposure demonstrated the AuNRs-loaded liposomes' sensitivity to NIR as a stimulus for controlled release, a characteristic that can be finely tuned for precision in drug delivery applications.

Enhancement of Pharmacological Payload Solubility

Melatonin (N-[2-(5-methoxy-1H-indol-3-yl)ethyl]acetamide) is a neurohormone secreted mainly by the pineal gland in mammals, and also in the retina.³² This hormone is crucial for regulating circadian rhythms, sleep-wake cycles, immune responses, and bone development, while also offering antioxidant benefits and suppressing tumor growth.^{29, 33} Despite its angiogenic and non-toxic characteristics enhancing its neuroprotective efficacy³⁴, melatonin's application is limited by its poor water solubility.^{35, 36} To address this, we utilized its amphiphilic nature to form inclusion complexes with cyclodextrins (CDs) by incorporating melatonin into CDs' hydrophobic cavities (Fig. 2A). CDs are cyclic oligosaccharides made from $(\alpha-1,4)$ -linked D-glucopyranose units, forming structures known as α -, β -, and γ -cyclodextrins. ^{37, 38} These molecules are characterized by a hydrophilic hydroxyl group exterior and a hydrophobic central cavity. This structure allows CDs to enhance drug solubility by encapsulating hydrophobic drug molecules within their nonpolar core, while the hydrophilic outer surface facilitates solubilization by interacting with water.^{39, 40} Based on its water solubility enhancement capabilities, we identified HPBCD, a derivative of β-cyclodextrin, to improve melatonin's solubility in water (Fig. 2A). To demonstrate the solubilization capacity of HPBCD for hydrophobic molecules, we chose Oil Red O as a representative hydrophobic compound (Fig. 2B). Initially, we prepared the inclusion complex of Oil Red O/HPBCD using rotary shaking and microwave irradiation to promote high yield. When Oil Red O was initially introduced into the aqueous HPBCD solution, a visible separation occurred between unencapsulated Oil Red O and HPβCD solution (i). After continued shaking and microwave agitation, we observed the assimilation of Oil Red O into the hydrophobic core of HPBCD via hydrophobic-hydrophilic interactions in a uniform solution (ii), indicating successful complexation. After desiccation to remove water and subsequent resuspension in chloroform, Oil Red O maintained its bright red coloration in chloroform (iii), confirming the structural integrity of the dye molecules throughout the complexation process.

To further understand drug/HP β CD complex formation, we simulated the equilibrium dynamics between a model drug and HP β CD. The model drug, depicted in green, represents its free, unbound state, while the unoccupied cyclodextrin appears as its free oligosaccharide form (Fig. 2C). The equilibrium is defined by

two constants K₁ and K₋₁, representing complex formation and dissociation, respectively.³⁹ We mapped the kinetic profile of a drug's interaction with cyclodextrin through the relative concentrations of each entity over time (Fig. 2C). The red line represents the concentration of unbound cyclodextrin, decreasing as it binds to the drug to form complexes. Conversely, the green line indicates the concentration of the free drug, diminishing as it becomes sequestered by cyclodextrin. The blue line marks the accumulation of the cyclodextrin-drug complex, increasing as complexation progresses and stabilizing when equilibrium is reached with the free drug and cyclodextrin. The dashed line represents the equilibrium point, showing when the free drug concentration and cyclodextrin-drug complex levels balance. Initially, the free drug concentration (green line) decreases as it forms complexes. Upon complexation, as the blue line illustrates, the solubility increases, surpassing the dashed line, leading to enhanced dissolution in the solution. For in vivo delivery, physiological conditions such as drug binding to cell membranes, diffusion, and rapid elimination of cyclodextrin can further shift the equilibrium in favor of drug release. Additionally, environmental factors like pH and temperature can influence this equilibrium.

The dissociation of the drug from HP- β -CD is primarily driven by concentration gradients after in vivo dilution, as seen with melatonin release, which we propose as a key factor influencing drug release in physiological conditions. To simplify the analysis of this process, we applied the classic Weibull model to predict the kinetics of drug release from the liposomes. We used a shape parameter, β =1.5, to describe the wear-out characteristic of drug release from liposomes and subsequent uptake or diffusion (Fig. 2D).⁴¹, ⁴² Upon NIR illumination and triggered drug release, the rate of drug release initially increased and then plateaued, suggesting that drug concentration in the system gradually reached saturation.

To validate the drug loading, we used UV-Vis spectrophotometry to measure encapsulation efficiency and loading capacity. We first confirmed melatonin's distinct absorption peak at 278 nm (Supplementary Fig. 1A). We then established a standard calibration curve based on the absorbance at this wavelength from a range of melatonin concentrations (0.0125 mM to 0.2 mM) (Supplementary Fig. 1B). Following the preparation of the melatonin/HPβCD complex, we analyzed the UV-Vis absorbance spectra of the initial melatonin concentration, the control HPβCD solution without melatonin, and the melatonin/HPβCD complex solution (Supplementary Fig. 1C). The encapsulation efficiency (EE%) was calculated to be 84.1%, while the melatonin loading capacity (LC), representing the amount of melatonin per unit weight of HPβCD, was determined to be 3.03%. These results align with typical cyclodextrin–guest complexes characteristics reported in the literature.⁴³ Following the investigation with the Calcein release (Fig. 1K), we applied the same NIR-triggered release approach to melatonin-encapsulated liposomes (Supplementary Fig.2). The melatonin release was tracked using UV-vis spectrophotometry, under

varying illumination times ranging from 100 to 400 seconds. Like dye release, a gradual increase in melatonin release was observed with increasing NIR exposure time, peaking between 300 and 400 seconds, confirming that AuNRs-loaded liposomes effectively respond to NIR.

In vitro Cytotoxicity Assessment

To assess the feasibility and compatibility of our melatonin/HPβCD AuNRs liposome nanocarriers for biomedical applications, we conducted cytotoxicity tests with in vitro cultured cells. Using two distinct cell lines—human corneal epithelial cells and human embryonic kidney (HEK293) cells—we evaluated cell viability employing the dual-colored Calcein-AM/ ethidium homodimer-1 (EthD-1) assay. Under fluorescence microscopy, the green fluorescence of Calcein-AM identified live cells, while the red fluorescence of Ethidium Homodimer-1 marked the dead cells (Fig. 2E and Supplementary Fig. 3A). The cell cultures were incubated with melatonin/HPβCD complex solutions, melatonin/HPβCD complex-loaded AuNR liposomes without NIR illumination, and with NIR illumination for 100 and 400 seconds (Fig. 2F and Supplementary Fig. 3B). After quantifying cell death rates across these groups, no significant differences were found, confirming adequate biocompatibility.

In Vivo Cytotoxicity Assessment: AuNRs Liposomes and NIR Illumination

To further evaluate the in vivo biocompatibility of our AuNRs liposome system as drug carriers and their potential tissue responses to NIR illumination, we analyzed the retinal tissue responses in wild-type mice using pure AuNRs-loaded liposomes without any drug. The experimental timeline from Day 0 to Day 15 began with an injection of AuNRs liposomes, followed by varying durations of NIR exposure (Fig. 3A). We dissected the mouse retinal tissues and stained the RGC cells with RNA binding protein with multiple splicing (RBPMS) in red and the activated glial cells with glial fibrillary acidic protein (GFAP) in green (Fig. 3B). We compared fluorescent microscopy images from three groups: mice that received a saline injection without NIR illumination (+ Saline, - NIR), those that received AuNRs liposome injection but without NIR illuminations (+ AuNRs Liposomes, - NIR), and those injected with AuNRs liposome and subjected to NIR illuminations (+ AuNRs Liposomes, + NIR). We observed minimal GFAP expression, which indicates glial activation, in the groups receiving both AuNRs liposomes and NIR illumination, compared to the saline control group. The morphology and cell numbers of RBPMS-stained RGCs remained consistent across all groups, suggesting AuNRs liposomes and NIR illumination did not negatively impact RGC density (Fig. 3B). Quantitative analysis of the fluorescent microscopy images showed no statistically significant differences in the normalized numbers of RGCs (Fig. 3C), the intensity

of GFAP fluorescence (Fig. 3D), and the depth of GFAP penetration (Fig. 3E) between the control group and those subjected to AuNRs liposomal and NIR.

NIR Enabled Neuroprotection in Glaucoma

Glaucoma is mainly characterized by the progressive degeneration of RGCs while elevated IOP is considered a predominant risk factor with a pathogenic mechanism involving axonal injury and RGC death.⁴⁴ Introducing ocular hypertension in rodent models with RGC degeneration features provided experimental models for the study of glaucoma.⁴⁵ Utilizing a previously established acute glaucoma mouse model with oil injection⁴⁶, we tested the neuroprotection efficacy of AuNRs liposome-delivered melatonin. At the outset (Day 0), mice received an injection of melatonin/HPβCD-loaded AuNRs liposomes to establish a protective environment in anticipation of induced glaucoma. An oil injection was then administered to create the acute glaucoma model, with concurrent IOP monitoring to validate induction and progression (Fig. 4A). All mice received intracameral injections of oil into the anterior chamber.

We monitored the IOP trends over 15 days for three groups: control mice with glaucoma (blue), glaucoma-induced mice with intravitreal melatonin/HPβCD-loaded AuNRs liposome injection without NIR illumination (yellow), and ones with intravitreal melatonin/HPβCD-loaded AuNRs liposome injection followed by 100-second NIR illumination for 4 times (red) (Fig. 4B). All groups showed a similar trend of IOP elevation following oil injection during the first three days (Fig. 4B). We compared the IOP measurements of the three different treatment groups at three-time points: Day 0, Day 6, and Day 15 (Fig. 4C). Before introducing acute glaucoma in vivo (Day 0), all groups started with a similar low IOP range (10 to 12 mmHg) as the same baseline. By Day 6, after introducing acute glaucoma, all groups exhibited significant IOP elevations but there was no statistically significant difference between the groups. Since glaucomatous neurodegeneration is a progressive process, we kept monitoring IOP across three groups and by Day 15, the group treated with melatonin/HPβCD-loaded AuNRs liposomes and NIR illuminations showed a notable decrease in IOP compared to the other two groups.

To investigate the cellular responses, we performed immunobiological staining and fluorescence microscopy on retina tissues from the three groups. The control group without treatment showed higher GFAP activity, indicating an increased glial response to the pathological state induced in the glaucoma model (Fig. 4D). When we examined the RGC morphology and density, we observed that the control and melatonin/HPβCD-loaded AuNRs liposome-only groups did not show a statistically significant change in RGC numbers while the melatonin/HPβCD-loaded AuNRs liposome with NIR illumination displayed a

higher RGC count (Fig. 4E). This indicates an enhancement in RGC survival following the NIR-triggered melatonin release. Although all treated groups exhibited increased GFAP intensity, those receiving NIR illumination had the least depth of GFAP expression (Fig. 4G), suggesting a mitigation of reactive gliosis compared to the other treatments.

Conclusion

In this study, we introduced a remotely controlled nanomaterial-based approach to mitigate the progression of neurodegenerative glaucoma. By incorporating AuNRs and cyclodextrin-encapsulated melatonin into temperature-responsive liposomal nanocarriers, we achieved controlled, multiple-dose release via NIR illumination and demonstrated its neuroprotection effect in glaucoma mouse models. This technology provides a localized treatment strategy, leveraging photothermal effects for reversible and accurate dosing for targeted therapy in ocular conditions. This on-demand release mechanism ensures precision in both timing and dosage of drug delivery, potentially enhancing therapeutic outcomes in targeted therapy.

Materials and Methods:

Synthesis of Photothermal Liposome preparation:

AuNRs (0.925 nM) with an average size of 10 nm were obtained from Nanopartz (Catalog No. AC12). (2-hydroxypropyl)-beta-cyclodextrin (HP-β-CD) was sourced from Accela ChemBio Inc. (Catalog No. SY004863). Melatonin and cholesterol were acquired from Thermo Scientific (Catalog Nos. 125360010 and A11470.18, respectively). Dipalmitoylphosphatidylcholine (DPPC) and 1,2-Distearoyl-sn-glycero-3phosphoethanolamine-polyethylene glycol 2000 (DSPE-PEG 2000) were purchased from Avanti Polar Lipids (Catalog Nos. 850355 and 880132P, respectively). The liposomes were constructed using a predefined lipid ratio of DPPC: cholesterol: DSPE-PEG 2000 (66.5:28.5:5). The lipids were initially dissolved in dichloromethane to create a homogeneous lipid solution. Subsequently, a mixture containing AuNRs and HP-β-CD-melatonin complex was prepared and introduced to the lipid solution. This mixture was subjected to vigorous vortexing at 3,000 rpm to ensure thorough mixing. Homogenization was achieved via sonication, utilizing an amplitude setting of 20% and employing an intermittent cycle of 10 seconds on and 15 seconds off over a 10-minute period. Following this, a second addition of the aqueous phase was added, accompanied by immediate vortexing to ensure the formation of a stable double emulsion. The resultant emulsion underwent vacuum evaporation for a duration of 30 minutes to remove any residual organic solvent, thereby finalizing the synthesis of the photothermal liposomes. Purification of the resulting liposome suspension was performed through centrifugation at 10,000 rpm for 7 minutes, followed by resuspension in distilled water to yield the final photothermal liposome product.

Particle size:

The distribution of liposome sizes and the average diameter were assessed using Nanoparticle Tracking Analysis (NTA) on a NanoSight NS300 system (Malvern Instruments), which features a 532 nm laser and a specialized sample chamber for precise measurements. Prior to analysis, liposome suspensions were diluted to a 1:1000 ratio in distilled water to ensure optimal particle movement and prevent coincidental counting. The diluted samples were then carefully loaded into the sample chamber using syringes, ensuring the chamber was filled to the tip to maintain consistent measurement conditions. Each sample underwent triplicate measurements at controlled room temperature to ascertain reproducibility and accuracy of the size distribution data.

Dye-release measurements using temperature:

Thermal release studies were conducted on liposomes encapsulating Calcein, which were synthesized at a 10 mM concentration within the initial aqueous phase according to previously established methods. The

measurements were initiated at 37 °C for ten minutes before increasing to 42 °C for an additional seventy minutes. Fluorescence readings were captured at five-minute intervals to determine the release kinetics. Fluorescence intensity of Calcein was quantified using a Cytation 5 Cell Imaging Multi-Mode Reader (BioTek, VT). The instrument settings were an excitation wavelength of 490 nm with emission detection at 520 nm for Calcein.

Cell Culture Biocompatibility Tests on Human Corneal Epithelial Cells:

Human Corneal Epithelial cells (HCECs) were cultured in Dulbecco's Modified Eagle Medium (DMEM) supplemented with GlutaMaxTM (Sigma Aldrich, Catalog No. D5796) and 5% fetal bovine serum. Cells were seeded into 24-well plates and were supplemented with 1 μ L of liposome/DMSO suspensions for 24 hours. Cell viability was assessed using Calcein-AM (2 μ L of 1 mg/mL per well; green fluorescence, Sigma-Aldrich, Catalog No. 17783) to denote live cells, while dead cells were identified by staining with Ethidium Homodimer-1 (2 μ L of 1 mg/mL per well; red fluorescence, Sigma-Aldrich, Catalog No. 46043). Fluorescence microscopy was performed using an Inverted microscope (Eclipse; Nikon, Melville, NY), where it captured fluorescent signals from cells in the presence and absence of liposomal incubation. Quantitative analysis of live and dead cells was conducted using ImageJ software. The cell death rate was determined as the ratio of dead cells to total cells, expressed as a percentage, calculated by the following formula: Deathrate (%) = $\frac{Dead\ cell\ numbers}{Total\ cell\ numbers}$ × 100%

Total cell numbers

Temperature Measurements of Gold and Water Under NIR Irradiation:

The photothermal properties of AuNRs were validated using a temperature measurement assay. An 808 nm NIR laser (Adjustable Lab 808nm 1W Infrared Laser, CivilLaser, Hangzhou, China) coupled with a precision temperature probe system (Iworx Systems, Dover, NH) served as the basis for monitoring. We assessed various concentrations of AuNRs, at 0.925 nM (1X), 2.31 nM (2.5X), and 4.63 nM (5X), alongside distilled water as a control. To obtain these concentrations, we centrifuged the original 1X AuNRs solution, concentrating it to final volumes of 0.400 mL and 0.200 mL for the 2.5X and 5X solutions, respectively, using the same centrifugation time and parameters as in liposomal fabrication. Each sample, with a volume of 50 μ L, was placed into a specifically designed chamber for analysis. Post-NIR laser irradiation, real-time temperature changes were recorded over a period of 100 seconds to evaluate the photothermal response.

Synthesis of Cyclodextrin Inclusion Complexes Using Microwave-Assisted Methods:

The synthesis of the melatonin/Oil Red O (Sigma Aldrich, Catalog No. O0625) and HP-β-CD inclusion complex was performed using microwave-assisted techniques. Initially, 10 mg of Oil Red O and 329 mg of HP-β-CD were dissolved in 5 mL of distilled water within screw-capped vials. These mixtures were agitated for 24 hours on a rotary shaker (Benchmark, Catalog No. 364008) at a controlled temperature of 37 °C and a speed of 300 rpm to ensure thorough homogenization. Subsequently, the solutions were subjected to microwave irradiation (Mainstays) at a power setting of 700 W for a duration of 60 seconds. Following microwave exposure, the solutions were allowed to dry in a desiccator for 36 hours at ambient temperature. The resultant inclusion complexes, observed in solid form, were then resuspended in chloroform for further analysis. To assess encapsulation efficiency, we measured the concentration of melatonin using UV-Vis spectrophotometry, following a quantification method reported in the literature. The encapsulation efficiency (EE, %) was determined using the formula:

$$EE\% = 100 \times (\frac{\textit{Amount of melatonin encapsulated}}{\textit{Total amount of melatonin added}}) \; .$$

Animals:

Wild-type C57BL/6J mice, sourced from the Jackson Laboratory (JAX), were selected for this study. These mice, aged 6-8 weeks and weighing 20-25 grams, were used in accordance with the animal protocol approved by the Institutional Animal Care and Use Committee (IACUC) at Binghamton University, ensuring compliance with all relevant regulations. Housing conditions for the mice included a maximum of four mice per cage, adherence to a 12-hour light/dark cycle, and unrestricted access to food and water.

Intravitreal Injection of Liposomes:

Liposomes were administered to the mice through intravitreal injection directly into the eyes. In this procedure, a finely pulled-glass micropipette was carefully positioned near the peripheral retina, just behind the ora serrata, and strategically angled to prevent any damage to the lens. Subsequently, 1 μ L of the liposomes was precisely injected into the vitreous body of the mice's eyes. Following the injection, an antibiotic ophthalmic ointment was applied to the surface of the cornea to prevent infection.

Intracameral injection of oil:

Induction of elevated IOP was achieved by injecting oil into the anterior chamber of the mice's eyes, utilizing a technique modified from the established microbead occlusion model.^{45, 48} Under anesthesia, the mice's corneas were delicately pierced with a 33g needle (CAD4113, Sigma), creating an entry point. Following this, 1-2 µL of oil was carefully injected into the anterior chamber. The mice received an

application of Vetropolycin antibiotic ointment (Dechra Veterinary Products, Overland Park, KS) for infection prevention. Post-procedure, the mice were placed on a heating pad to facilitate recovery.

NIR Laser Treatment in Vivo:

C57BL/6J mice underwent treatment using an 808 nm NIR Laser. Following anesthesia, mice were securely positioned within a restraint device, and the laser was precisely aligned in front of the eye, maintaining a 5 mm distance. Both eyes remained open throughout the treatment, which was well tolerated. The irradiation protocol involved exposure to an 808 nm wavelength for 100 seconds, with a power intensity of 11.2 mW targeting the corneal surface. This treatment was administered every three days, culminating in a 14-day period, with perfusion conducted on the final day.

Immunohistochemistry:

For the immunostaining process, the animals were euthanized using an overdose of anesthesia and subsequently perfused transcardially with phosphate-buffered saline (PBS), followed by 4% paraformaldehyde (PFA, Sigma) to fix the tissues. The retinal tissues were then dissected and post-fixed in 4% PFA for an overnight period at 4°C. To achieve cryoprotection, the dissected tissues were immersed in a 30% sucrose solution prepared in PBS for 24 hours. Following this, the samples were embedded in Optimal Cutting Temperature compound (Tissue Tek) using dry ice and sectioned into 20 µm slices. The retina sections were washed in PBS and then blocked in a solution composed of PBS, 1% Triton X-100, and 1% bovine serum albumin (BSA) for 30 min at room temperature. Primary antibodies, diluted in the blocking buffer, were applied to the sections and incubated overnight at room temperature. This step was followed by three PBS washes, each lasting 10 minutes. Subsequently, secondary antibodies diluted at a 1:1000 ratio in PBS were applied and left to incubate for 2 hours at room temperature. After undergoing three additional PBS washes, the retinas were prepared for microscopy by mounting them using Fluoromount-G (Southern Biotech, Cat. No. 0100-01). Imaging was performed using a NIKON Inverted Microscope. For the evaluation of RGC loss, quantitative analyses were conducted using the Image J software.

Data Analysis:

Normality and variance similarity assessments, crucial prerequisites for conducting parametric tests, were exclusively performed using GraphPad Prism. Should these assessments reveal that the data did not meet the criteria for parametric testing, non-parametric tests were subsequently employed. For analysis of multiple groups involved either one-way or two-way ANOVA. Post hoc comparisons were initiated only upon observing statistical significance in the primary analysis. The presentation of error bars in all figures

corresponds to the mean \pm S.E.M. In the animal studies, mice varied in litters, body weights, and sexes, and were randomized across different treatment groups without the application of further randomization methods. The experimental data points represent individual measurements or observations, detailed within the captions of the corresponding figures. All statistical analyses were conducted utilizing GraphPad Prism 10, establishing significance at P values less than 0.05. Significance levels were denoted as follows: * for $0.01 \le p < 0.05$, ** for $0.001 \le p < 0.01$, *** for $0.0001 \le p < 0.001$, and "NS" indicating non-significance.

Author contributions:

D.M., Q.W., and S.R. conceptualized the photothermal liposome project. The in vitro experiments were executed by D.M., X.X., B.M., K.R., Q.W. and S.R. In vivo injections were conducted by Q.W. Measuring intraocular pressure was carried out by D.M. and Q.W. Analysis and imaging were collaboratively performed by D.M., Q.W., S.R., S.H., E.H., G.J., X.X., J.A., R.X. The manuscript was primarily authored by D.M., Q.W., and S.R.

Conflicts of interest:

The authors declare no conflicts of interest.

Data availability

All data are available in the main text or the ESI, with additional data provided upon request.

Acknowledgments:

We appreciate the support and advance from Dr. Md Mofizur Rahman, Benjamin Morrow, Kristine Rowe, Winny Guan Zheng, Julianna Ayres, Dr. Kaimin Ye, and Dr. Yuan Wan. This study received funding from the National Institutes of Health (R00MH120279), the National Science Foundation Faculty Early Career Development Program (CAREER, 2239030), the Brain & Behavior Research Foundation Young Investigator Grant (29878), Faculty Startup Funds from Binghamton University, and Binghamton University Small Scale Systems Integration and Packaging (S3IP) Center of Excellence (ADLG 274 for Q.W. and ADLG 267 for S.R.). We also thank the core facilities and the Laboratory of Animal Service at Binghamton University for their assistance.

References

- 1. R. M. Sappington, B. J. Carlson, S. D. Crish and D. J. Calkins, *Invest Ophthalmol Vis Sci*, 2010, **51**, 207-216.
- 2. D. D. Nguyen, C.-H. Yao, S. J. Lue, C.-J. Yang, Y.-H. Su, C.-C. Huang and J.-Y. Lai, *Chemical Engineering Journal*, 2023, **451**, 138620.
- 3. G. Scuderi, S. Fragiotta, L. Scuderi, C. M. Iodice and A. Perdicchi, *Eye Brain*, 2020, **12**, 33-44.
- 4. R. H. Sim, S. R. Sirasanagandla, S. Das and S. L. Teoh, *Nutrients*, 2022, 14, 534.
- 5. D. Schmidl, L. Schmetterer, G. Garhöfer and A. Popa-Cherecheanu, *J Ocul Pharmacol Ther*, 2015, **31**, 63-77.
- 6. H. Kumar, T. Mansoori, G. B. Warjri, B. I. Somarajan, S. Bandil and V. Gupta, *Indian J Ophthalmol*, 2018, **66**, 1539-1553.
- 7. B. C. H. Ang, S. Y. Lim, B. K. Betzler, H. J. Wong, M. W. Stewart and S. Dorairaj, *Bioengineering* (*Basel*), 2023, **10**.
- 8. J.-Y. Lai, L.-J. Luo and D. D. Nguyen, *Chemical Engineering Journal*, 2020, **402**, 126190.
- 9. L.-J. Luo, D. D. Nguyen and J.-Y. Lai, *Theranostics*, 2021, **11**, 5447-5463.
- 10. V. Andrés-Guerrero, M. Vicario-de-la-Torre, I. T. Molina-Martínez, J. M. Benítez-del-Castillo, J. García-Feijoo and R. Herrero-Vanrell, *Investigative Ophthalmology & Visual Science*, 2011, **52**, 3548-3556.
- 11. D. D. Nguyen and J.-Y. Lai, *Polymer Chemistry*, 2020, **11**, 6988-7008.
- 12. Y. T. Liao, C. H. Lee, S. T. Chen, J. Y. Lai and K. C. Wu, *J Mater Chem B*, 2017, **5**, 7008-7013.
- 13. C. H. Lee, Y. J. Li, C. C. Huang and J. Y. Lai, *Nanoscale*, 2017, **9**, 11754-11764.
- 14. S. K. Kushwaha, P. Saxena and A. Rai, *Int J Pharm Investig*, 2012, **2**, 54-60.
- 15. J.-Y. Lai, Drug design, development and therapy, 2013, 7, 1273-1285.
- 16. J. Y. Lai and L. J. Luo, Eur J Pharm Biopharm, 2017, **113**, 140-148.
- 17. Y. Cao, C. Zhang, W. Shen, Z. Cheng, L. L. Yu and Q. Ping, *J Control Release*, 2007, **120**, 186-194.
- 18. L. Liu, W. Yao, Y. Rao, X. Lu and J. Gao, *Drug Deliv*, 2017, **24**, 569-581.
- 19. S. Zhuo, F. Zhang, J. Yu, X. Zhang, G. Yang and X. Liu, *Molecules*, 2020, **25**, 5649.
- 20. T. Lajunen, R. Nurmi, L. Kontturi, L. Viitala, M. Yliperttula, L. Murtomäki and A. Urtti, *Journal of Controlled Release*, 2016, **244**, 157-166.
- 21. M. Afarid, S. Mahmoodi and R. Baghban, *J Nanobiotechnology*, 2022, **20**, 361.
- 22. I. J. Rad, L. Chapman, K. R. Tupally, M. Veidt, H. Al-Sadiq, R. Sullivan and H. S. Parekh, *Theranostics*, 2023, **13**, 3582-3638.
- 23. Q. Zhu, S. Xiao, Z. Hua, D. Yang, M. Hu, Y.-T. Zhu and H. Zhong, *International Journal of Medical Sciences*, 2021, **18**, 109-119.
- 24. W. Zhao, Y. Zhao, Q. Wang, T. Liu, J. Sun and R. Zhang, *Small*, 2019, **15**, e1903060.
- 25. H. A. M. Abdelmohsen, N. A. Copeland and J. G. Hardy, *Drug Delivery and Translational Research*, 2023, **13**, 2159-2182.
- 26. S. Rao, R. Chen, A. A. LaRocca, M. G. Christiansen, A. W. Senko, C. H. Shi, P.-H. Chiang, G. Varnavides, J. Xue, Y. Zhou, S. Park, R. Ding, J. Moon, G. Feng and P. Anikeeva, *Nature Nanotechnology*, 2019, **14**, 967-973.
- 27. H. H. Nguyen, J. Park, S. Kang and M. Kim, Sensors, 2015, 15, 10481-10510.
- 28. K. M. Mayer and J. H. Hafner, *Chemical Reviews*, 2011, **111**, 3828-3857.
- 29. D. Gubin and D. Weinert, *Neural Regen Res*, 2022, **17**, 1759-1760.
- 30. M. Alrahili, V. Savchuk, K. McNear and A. Pinchuk, Scientific Reports, 2020, 10, 18790.
- 31. S. Choi, B. Kang, E. Yang, K. Kim, M. K. Kwak, P.-S. Chang and H.-S. Jung, *Scientific Reports*, 2023, **13**, 4728.
- 32. J. Blasiak, R. J. Reiter and K. Kaarniranta, *Oxid Med Cell Longev*, 2016, **2016**, 6819736.

- 33. M. Terauchi, A. Tamura, S. Yamaguchi and N. Yui, *Int J Pharm*, 2018, **547**, 53-60.
- 34. Y. Potes, C. Cachán-Vega, E. Antuña, C. García-González, N. Menéndez-Coto, J. A. Boga, J. Gutiérrez-Rodríguez, M. Bermúdez, V. Sierra, I. Vega-Naredo, A. Coto-Montes and B. Caballero, *Int J Mol Sci*, 2023, **24**.
- 35. A. Sakellaropoulou, A. Siamidi and M. Vlachou, *Molecules*, 2022, 27, 445.
- 36. R. Ferrero, S. Pantaleone, M. Delle Piane, F. Caldera, M. Corno, F. Trotta and V. Brunella, *Molecules*, 2021, **26**.
- 37. R. Challa, A. Ahuja, J. Ali and R. K. Khar, AAPS PharmSciTech, 2005, 6, E329-357.
- 38. D. D. Gadade and S. S. Pekamwar, *Adv Pharm Bull*, 2020, **10**, 166-183.
- 39. V. J. Stella, V. M. Rao, E. A. Zannou and V. V. Zia, *Adv Drug Deliv Rev*, 1999, **36**, 3-16.
- 40. S. Swaminathan, R. Cavalli and F. Trotta, *Wiley Interdiscip Rev Nanomed Nanobiotechnol*, 2016, **8**, 579-601.
- 41. C. Corsaro, G. Neri, A. M. Mezzasalma and E. Fazio, *Polymers*, 2021, 13, 2897.
- 42. V. Papadopoulou, K. Kosmidis, M. Vlachou and P. Macheras, *Int J Pharm*, 2006, **309**, 44-50.
- 43. S. Peimanfard, A. Zarrabi, F. Trotta, A. Matencio, C. Cecone and F. Caldera, *Pharmaceutics*, 2022, **14**, 1059.
- 44. R. Russo, G. P. Varano, A. Adornetto, C. Nucci, M. T. Corasaniti, G. Bagetta and L. A. Morrone, *Eur J Pharmacol*, 2016, **787**, 134-142.
- 45. F. Tian, Y. Cheng, S. Zhou, Q. Wang, A. Monavarfeshani, K. Gao, W. Jiang, R. Kawaguchi, Q. Wang, M. Tang, R. Donahue, H. Meng, Y. Zhang, A. Jacobi, W. Yan, J. Yin, X. Cai, Z. Yang, S. Hegarty, J. Stanicka, P. Dmitriev, D. Taub, J. Zhu, C. J. Woolf, J. R. Sanes, D. H. Geschwind and Z. He, *Neuron*, 2022, **110**, 2607-2624.e2608.
- 46. J. Zhang, L. Li, H. Huang, F. Fang, H. C. Webber, P. Zhuang, L. Liu, R. Dalal, P. H. Tang, V. B. Mahajan, Y. Sun, S. Li, M. Zhang, J. L. Goldberg and Y. Hu, *eLife*, 2019, **8**, e45881.
- 47. A. Zafra-Roldán, S. Corona-Avendaño, R. Montes-Sánchez, M. Palomar-Pardavé, M. Romero-Romo and M. T. Ramírez-Silva, *Spectrochimica Acta Part A: Molecular and Biomolecular Spectroscopy*, 2018, **190**, 442-449.
- 48. J. Zhang, L. Li, H. Huang, F. Fang, H. C. Webber, P. Zhuang, L. Liu, R. Dalal, P. H. Tang, V. B. Mahajan, Y. Sun, S. Li, M. Zhang, J. L. Goldberg and Y. Hu, *Elife*, 2019, **8**.

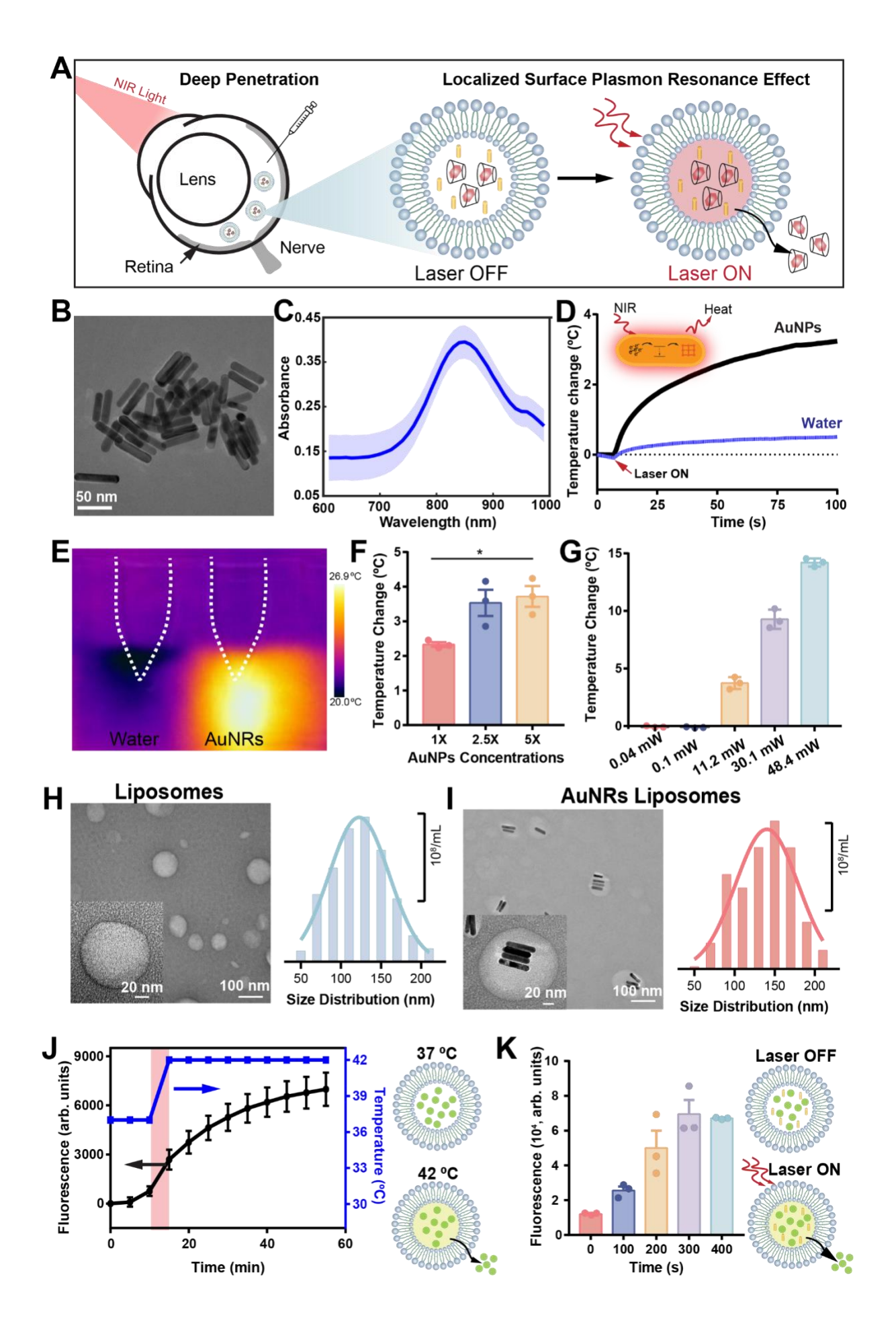


Figure 1 (A) A schematic illustration of the designed near infrared (NIR)-light-activated liposome delivery system. In the absence of NIR light (LASER OFF), melatonin-cyclodextrin complex encapsulated nanoscale liposomes with remain stable. Upon NIR light exposure (LASER ON), the liposomes release melatonin through a localized surface plasmon resonance effect, allowing the drug to diffuse into the vitreous humor of the eye. (B) Transmission electron microscopy (TEM) image of uniformly shaped gold nanorods (AuNRs). (C) Absorbance spectrum of AuNRs solutions. (Line: mean, shadow: S.D.) (D) Photothermal response of AuNRs solutions and water under NIR light illumination (11.2 mW, 100 seconds). The black curve represents the temperature increase of AuNRs upon NIR exposure. The blue dotted line and associated markers display the temperature change in water. The inset illustrates the mechanism of NIR-induced heat generation by AuNRs. (E) Thermal imaging of NIRstimulated AuNRs solutions at 11.2 mW after 100 s. (F-G) Temperature changes of AuNRs solutions at different gold concentrations at 11.2 mW (F) and at different NIR illumination intensities of 0.04, 0.10, 11.2, 30.1 and 48.4 mW (G). Data are represented as means \pm S.D. (n = 3 independent samples). Significant difference: *p < 0.05; (H-I) TEM images and size distributions of liposome without AuNRs and liposome with AuNRs with the average sizes of 121.7 ± 5.0 and 129.8 ± 13.6 nm, respectively; (J) Temperature release of fluorescent Calcein dye from the liposomes from 37 to 42 °C. Data are represented as means \pm SEM. (n = 3 independent samples); (K) NIR-triggered release of fluorescent Calcein dye from liposomes with a series of illumination times ranging from 100 seconds to 400 seconds at 11.2 mW. Data are represented as means \pm SEM (n = 3 independent samples).

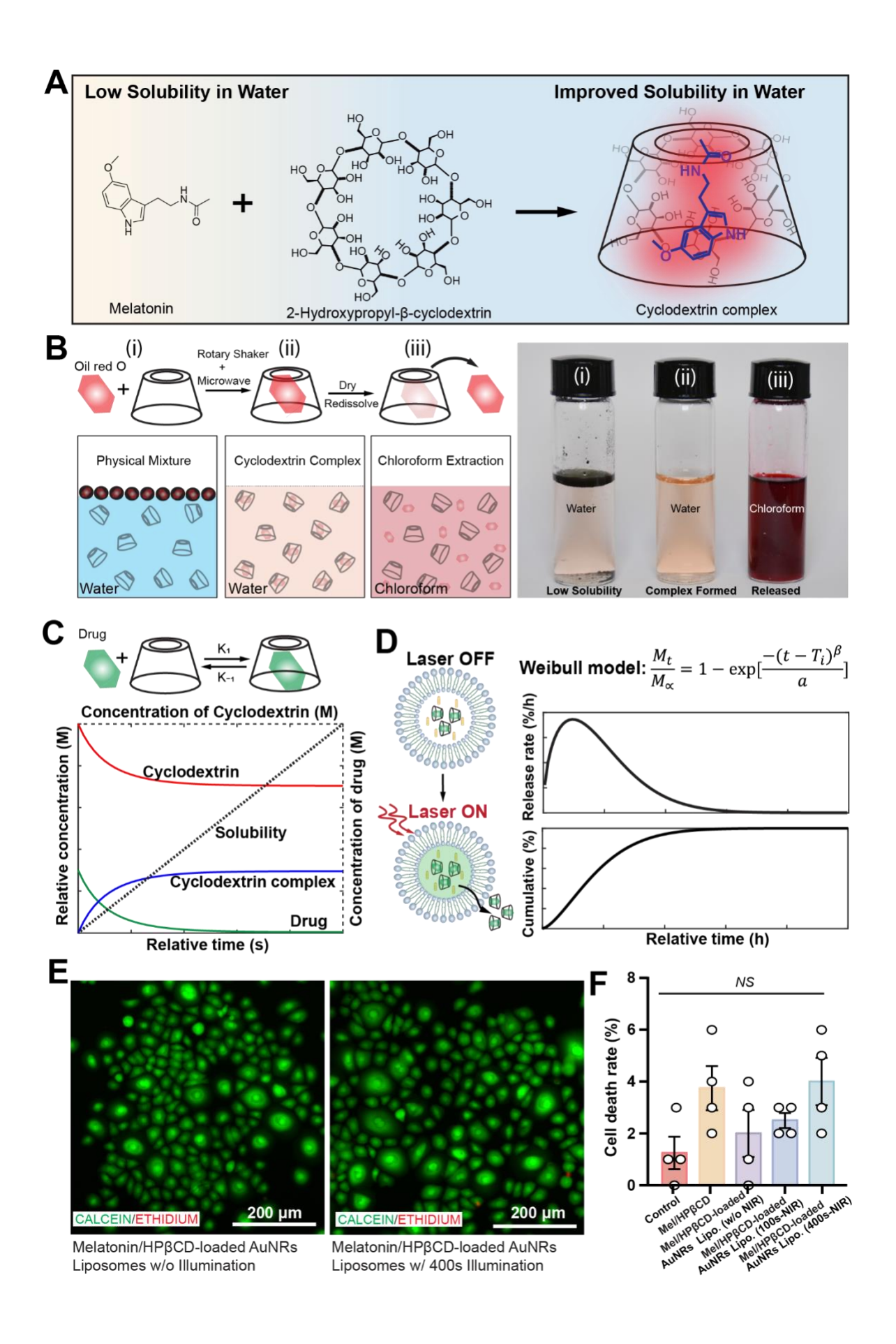


Figure 2 (A) Structural representation of melatonin and 2-Hydroxypropyl-β-cyclodextrin (HPβCD) forming an inclusion complex to improve the solubility in water. (B) Oil Red O as an exemplary hydrophobic compound was used to demonstrate the solubilization capabilities of HPBCD in water. (i) Initially, the mixture of Oil Red O and HPBCD showed a visible separation of unencapsulated Oil Red O and the HPBCD solution. (ii) After rotary shaking for 24 hours followed by microwave irradiation for 60 s, the Oil Red O was assimilated into the hydrophobic core of HPβCD via hydrophobic-hydrophilic interactions, resulting in a uniform solution and suggesting successful complexation. (iii) Following 36 hours of desiccation and subsequent resuspension in chloroform, the bright red coloration confirmed the unaltered structural composition and integrity of Oil Red O throughout the formation of the inclusion complex; (C) The interaction of a model drug with cyclodextrin to form an inclusion complex with a binding constant, K. (D) Modulation of drug release kinetics from liposomes using the Weibull Model under NIR laser stimulation. (E-F) Representative fluorescent microscopy images (E) and cell death quantification (F) assess the cytotoxicity impact of liposomes on human corneal epithelial cells, under conditions of melatonin/HPBCD AuNRs liposome in the presence or absence of NIR illuminations (11.2) mW, 400 seconds). Live cells are identified by Calcein-AM green staining, whereas dead cells are marked with red ethidium homodimer-1 staining. Data are represented as means \pm SEM (n = 4 independent samples). NS = no significant difference.

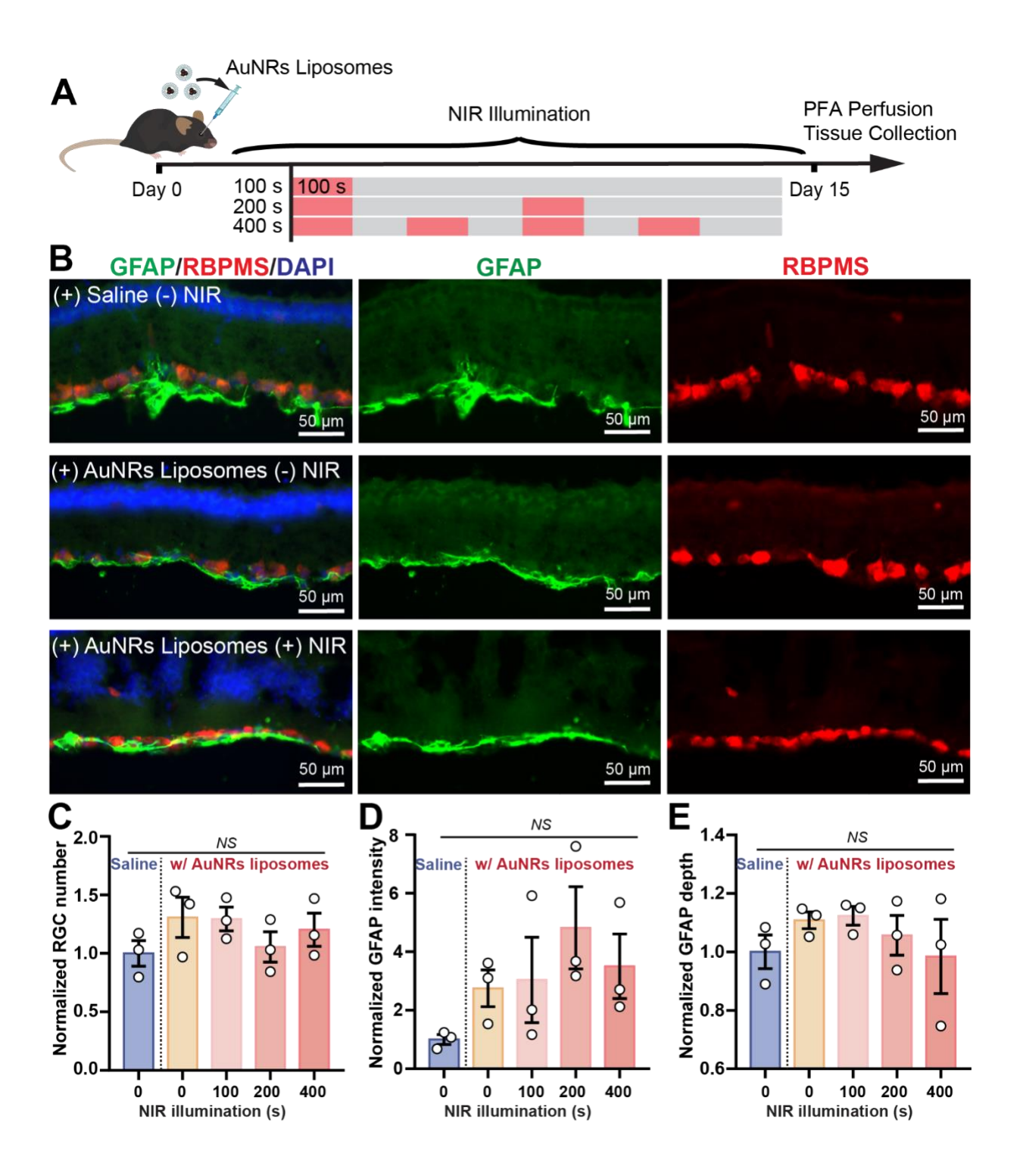


Figure 3 (A) The experimental timeline of AuNRs liposome injection and NIR illumination in vivo. (B) Representative images of fluorescent microscopy images of retinal tissues with immunohistochemical staining. Tissues are stained for glial fibrillary acidic protein (GFAP, green), RNA binding protein with multiple splicing (RBPMS, red), 4',6-diamidino-2-phenylindole (DAPI, blue); (C-E) Quantification assessment of normalized retinal ganglion cell (RGC) numbers, GFAP intensity and GFAP depth. Data are represented as means \pm SEM (n = 3 eyes). NS = no significant difference.

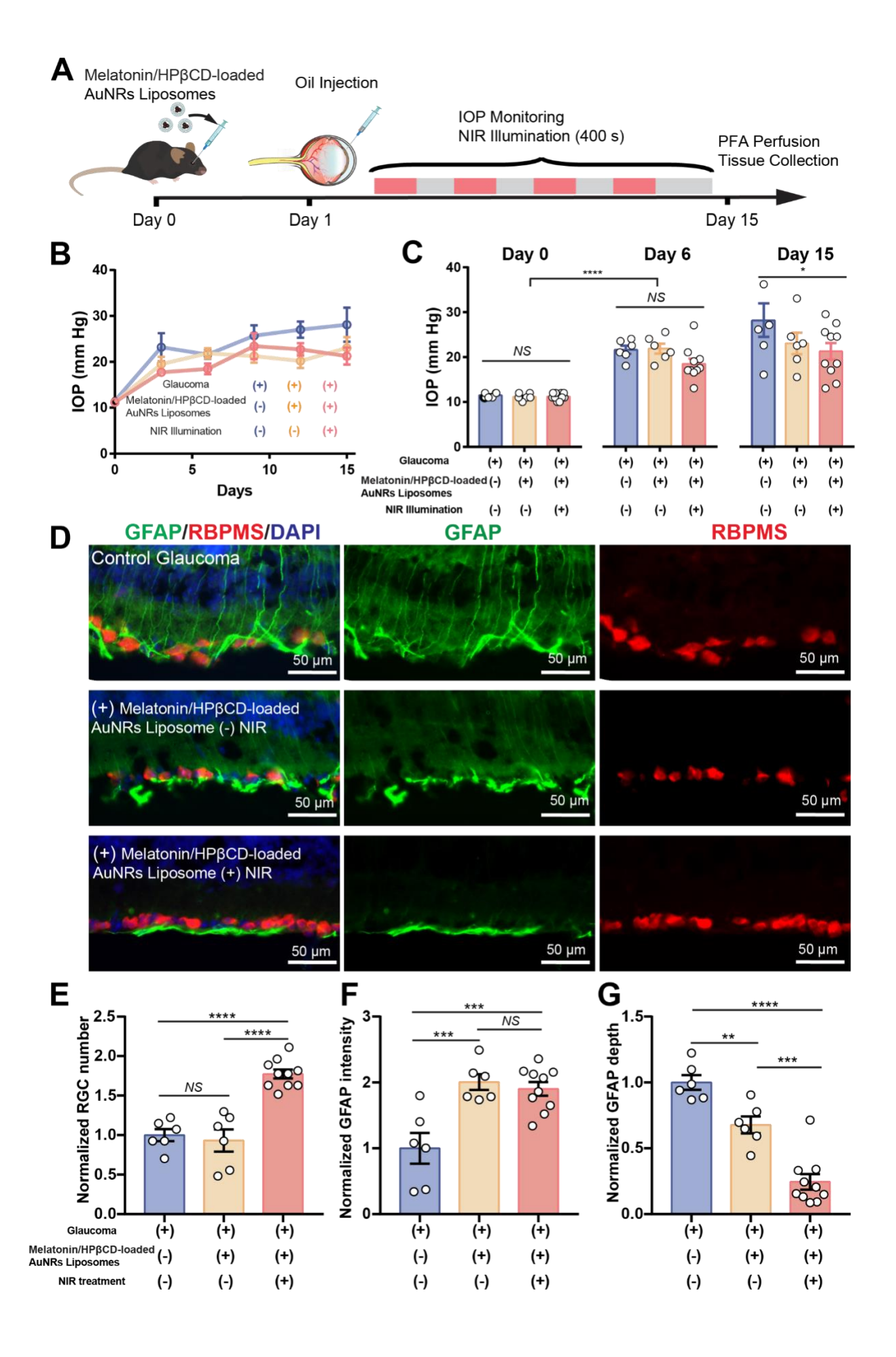


Figure. 4 (A) Schematic of the in vivo experimental timeline, initiating with the injection of melatonin/HPβCD AuNRs liposomes carrying the melatonin-HPβCD complex, followed by oil injection to introduce acute glaucoma and concluded with tissue collection. (B-C) Comparison of the measured intraocular pressure (IOP) in mice. The group of mice only received oil injection, but no melatonin/HPβCD AuNRs liposomes nor NIR treatment was the control group (blue). One group of glaucoma mice injected with melatonin/HPβCD AuNRs liposomes carrying melatonin-HPβCD complex received NIR illumination (red) while another group did not receive NIR illumination (yellow). Data are represented as means \pm SEM (n = 10 eyes for NIR treatment group and n=6 eyes for the other groups). Significant difference: *p < 0.05; ****p < 0.0001; NS = no significant difference. (D) Representative fluorescent microcopy images of mouse retina tissues from three groups. The tissues were immunohistochemically stained for GFAP (green), RBPMS (red) and DAPI (blue). (E-F) Quantification assessment of normalized RGC numbers, GFAP intensity and GFAP depth from the fluorescent microscope images. Data are represented as means \pm SEM (n = 10 eyes for NIR treatment group and n=6 eyes for the other groups). Significant difference: *p < 0.05; ***p < 0.01; ****p < 0.001; *****p < 0.0001; NS = no significant difference.